Glare Pattern Depiction: High-Fidelity Physical Computation and Physiologically-Inspired Visual Response

YUXIANG SUN*, University of Waterloo, Canada
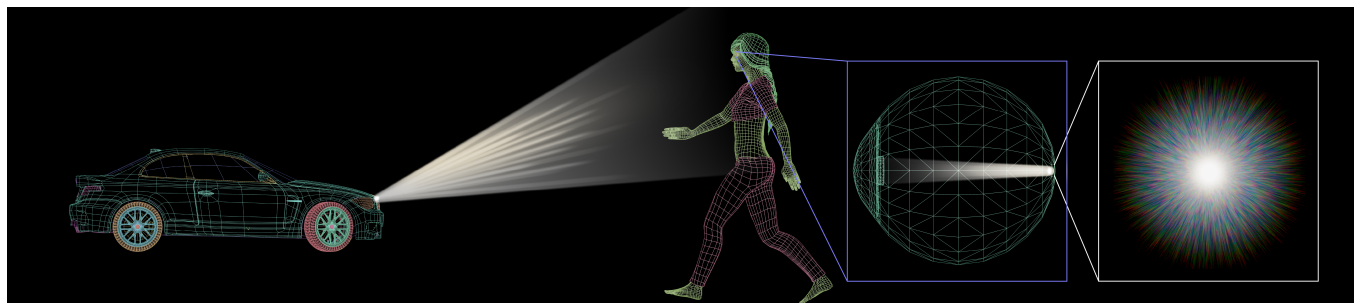GLADIMIR V. G. BARANOSKI, University of Waterloo, Canada

Fig. 1. A night scene (rendered in wireframe mode) illustrating the occurrence of the glare phenomenon. Since the luminous intensity of the car headlight is markedly stronger than its background, the observer sees a pattern consisting of a set of dense spikes radiating from the center of the light source. This pattern is elicited by diffraction happening inside the observer's eyeball. Assets: "Car Demo" (Mike Pan, CC0), "Scene Illumination Collection" (pikisuperstar / Freepik), "Dwarf Walk – woman" (rosaliarenda, CC BY, Sketchfab), and "Human Eye" (DEGUIDER, CC BY, Sketchfab).

When observing an intense light source, humans perceive dense radiating spikes known as glare/starburst patterns. These patterns are frequently used in computer graphics applications to enhance the perception of brightness (*e.g.*, in games and films). Previous works have computed the physical energy distribution of glare patterns under daytime conditions using approximations like Fresnel diffraction. These techniques are capable of producing visually believable results, particularly when the pupil remains small. However, they are insufficient under nighttime conditions, when the pupil is significantly dilated and the assumptions behind the approximations no longer hold. To address this, we employ the Rayleigh–Sommerfeld diffraction solution, from which Fresnel diffraction is derived as an approximation, as our baseline reference. In pursuit of performance and visual quality, we also employ Ochoa's approximation and the Chirp Z transform to efficiently generate high-resolution results for computer graphics applications. By also taking into account background illumination and certain physiological character-istics of the human photoreceptor cells, particularly the visual threshold of light stimulus, we propose a framework capable of producing plausible visual depictions of glare patterns for both daytime and nighttime scenes.

CCS Concepts: • **Computing methodologies** → **Rendering**; *Perception*.

Additional Key Words and Phrases: Rendering, Perception, Starburst, Glare, Diffraction, Human Visual System, Tone Mapping

---

*Corresponding author

Authors' Contact Information: Yuxiang Sun, University of Waterloo, Waterloo, Canada, y476sun@uwaterloo.ca; Gladimir V. G. Baranoski, University of Waterloo, Waterloo, Canada, gvgbaran@uwaterloo.ca.

1 Introduction

The stylized representations of stars usually contain multiple spikes that emanate from a bright spot. In real life, these spikes result from the diffraction of light waves in the camera imaging system [Lendermann et al. 2018]. Although the structure of the eyeball is different from that of a camera, the human visual system (HVS) is also affected by the diffraction during imaging. The pattern observed from an intense light source by the human eye consists of hundreds of dense spikes radiating from the source as illustrated in Fig. 1.

The point spread function (PSF) can be employed to describe how the light from a point light source is distributed (spread) across the retina [Ritschel et al. 2009; Spencer et al. 1995; Yang et al. 2008]. Accordingly, it has been used to quantitatively characterize the glare pattern in previous related works [Luidolt et al. 2020; Ritschel et al. 2009; Spencer et al. 1995; van den Berg et al. 2005].

The mechanism behind the glare phenomenon is complex and in-volves varied terminology [Mainster and Turner 2012]. Some works use the term starburst [Rubinstein 2019; Xu et al. 2018, 2019] or ciliary corona [Simpson 1953; van den Berg et al. 2005] to visually describe the phenomenon. Others broadly use the word glare [Kaki-moto et al. 2004; Ritschel et al. 2009; Spencer et al. 1995] since such a pattern is only observed around bright light sources.

In this work, the expression glare pattern is employed in connec-tion with the process by which the optical structure of the human eye causes a pattern similar to the one depicted in Fig. 1, which is quantitatively described by the PSF. The term glare phenomenon, on the other hand, refers to the observable event in which an average human observer perceives the aforementioned pattern only around a bright light source. The use of the term "phenomenon" considers factors beyond the PSF, such as background illumination and the

light intensity threshold of the photoreceptor cells, distinguishing it from the use of the term "pattern." The significance of these aspects will be discussed in Section 7. Additionally, it is worth noting that human observers may also perceive other visual effects, such as halos and blooms, around bright light sources [Spencer et al. 1995]. Their simulation, however, is beyond the scope of this work.

Driving is a classic scenario for the glare phenomenon to occur. On a sunny day, a driver may observe the pattern on a bright spot on the windows and chassis of other cars on the road. The specular reflection of sunlight induces this bright spot and can be classified as a secondary light source. In the nighttime, a driver may observe such a pattern from a streetlight or a headlight of an oncoming car as illustrated in Fig. 1. The glare phenomenon affects driving safety by overexposing the environment and reducing its contrast.

It is challenging to reproduce the glare phenomenon using traditional computer graphics techniques based on geometric (ray) optics since the pattern formed by hundreds of spikes results from diffraction, a wave optics phenomenon that can be associated with a high spatial frequency [Goodman 2017]. Moreover, the phenomenon occurs instantaneously and, thus, also has a high temporal frequency. This aspect challenges the HVS adaptation to light intensity variations, notably in driving situations [Grimes et al. 2018], and makes the design of physiologically-based algorithms difficult.

Relevant efforts have been devoted to the study of the glare phenomenon in computer graphics and related fields [Kakimoto et al. 2004; Luidolt et al. 2020; Nakamae et al. 1990; Ritschel et al. 2009; Rokita 1993; Shinya et al. 1989; Spencer et al. 1995; van den Berg et al. 2005]. However, the focus of previous works has been on the shape of the pattern, overlooking background illumination and the physiological characteristics of the photoreceptor cells, which affect the visibility of the pattern [Mainster and Turner 2012]. Notably, the works of Spencer et al. [1995] and Luidolt et al. [2020] did consider, to some extent, the role of the photoreceptor cells.

To address this gap, we build upon algorithms proposed by previous works while considering more closely the role played by the HVS, resulting in a framework for the plausible depiction of glare patterns. The proposed framework comprises two main stages, henceforth referred to as the propagation and response stages. The former simulates the light travelling from the front of the eyeball to the retina, while the latter computes the retinal response elicited by the light stimulus.

In the propagation stage, we employ the Rayleigh-Sommerfeld diffraction theory (with Ochoa's approximation) [Shen and Wang 2006] to enhance the physical correctness of the simulated patterns and the Chirp Z transform [Hu et al. 2020] to increase their resolution. In the response stage, we propose a novel physiologically-inspired algorithm, derived through a data-driven modeling process based on empirical measurements by Ferwerda et al. [1996], to approximate human brightness perception from luminance.

The remainder of this paper is organized as follows. In Section 2, we briefly examine previous works in related areas. In Section 3, we concisely review physiological aspects and methodologies relevant to this research. In Section 4 and 5, we describe the proposed framework and provide some implementation details. In Section 6, we assess theoretical aspects associated with the propagation stage. In Section 7, we present our simulation results obtained through the

response stage and discuss the plausibility and applicability of the proposed framework. Finally, in Section 8, we indicate directions for future investigations and conclude the paper.

2 Related Work

In the 1950s, Simpson [1953] observed colored rings around lamps similar to atmospheric phenomena such as haloes and coronas. He classified the patterns into three categories: Descartes corona, lenticular halo, and ciliary corona (the primary focus of this work). Through detailed observations, he also speculated that the ciliary corona pattern is caused by a uniform distribution of particles in the eye. Since then, these patterns have attracted the attention of researchers from different fields, including computer graphics.

In the 1990s, the glare phenomenon and high dynamic range (HDR) were often associated with each other [Spencer et al. 1995]. Glare originates from bright light sources [Ritschel et al. 2009]. Accordingly, a large range of illumination intensity is required to render this phenomenon properly. The dynamic range of an image is usually computed by dividing its brightest pixel by its darkest pixel. The ratio for traditional low dynamic range (LDR) images is usually $256 : 1$, while HDR images have a significantly larger ratio (*e.g.*, $10^6 : 1$) [Banterle et al. 2018]. As stated by Ritschel et al. [2009], besides the use of tone mapping techniques to map one set of colors to another to approximate the appearance of HDR images, one can apply a glare pattern to an LDR image to give the audience an HDR perception of a given scene.

2.1 Pattern Reproduction

Shinya et al. [1989] used star-like lines to increase perceived brightness when rendering transparent objects. They analyzed the structure of the "cross-screen filter" used by photographers, and used it to generate patterns similar to those captured by the cameras. When Nakamae et al. [1990] simulated driving at night, they accounted for the diffraction pattern produced by street lights due to eyelashes. Rokita [1993] claimed that Nakamae et al.'s simulations did not take into account the internal structure of the eye, and proposed an algorithm based on Simpson's observations. His improved algorithm produced rendering results that more closely approximated what humans observe rather than what cameras capture.

Spencer et al. [1995] systematically summarized the structure of the eyeball and proposed a method of generating glare accordingly. Compared to the previous works, their method pioneered the incorporation of physiological factors in glare simulation. They took into account two types of photoreceptor cells: cones and rods.

Kakimoto et al. [2004] proposed the use of Fourier optics (wave optics) for simulating glare patterns. They believed that the pattern is the result of the Fraunhofer diffraction of light at given apertures or obstacles. Their work only considered the shape of eyelashes and pupils, not the lens fiber or particles in the eyeball. Subsequently, van den Berg et al. [2005] were the first to simulate the pattern based on particles in an eyeball. Their results have significantly denser spikes compared to the previous results mentioned earlier [Kakimoto et al. 2004; Nakamae et al. 1990; Rokita 1993; Shinya et al. 1989; Spencer et al. 1995]. Ritschel et al. [2009] combined previous works [Kakimoto et al. 2004; van den Berg et al. 2005] and used

Fourier optics to simulate particles in the eyeball while also adding a temporal factor. Luidolt et al. [2020] brought the application of glare to virtual reality while incorporating the color shift due to night vision and visual acuity reduction in their simulations.

2.2 Human Visual System and Luminance Perception

In terms of luminance range, the human eye detects from 10^{-6} to 10^8 Nits, a full 14 orders of magnitude [Ferwerda et al. 1996]. In order to display what our eyes can see (especially details or high-frequency signals) on LDR screens, one can employ tone mapping algorithms. Some of them are physiologically based and others are not. Here, we briefly comment on three seminal papers on this topic.

Tumblin and Rushmeier [1993] proposed a mapping based on subjective brightness. When a person perceives the same brightness in the real world and on the monitor, the mapping is established via the corresponding luminance. However, this method reduces the visibility of dark areas. In the following year, Ward [1994] proposed a contrast-based algorithm that preserves visibility. Afterwards, Ferwerda et al. [1996] investigated the structure of the HVS and improved the contrast-based algorithm.
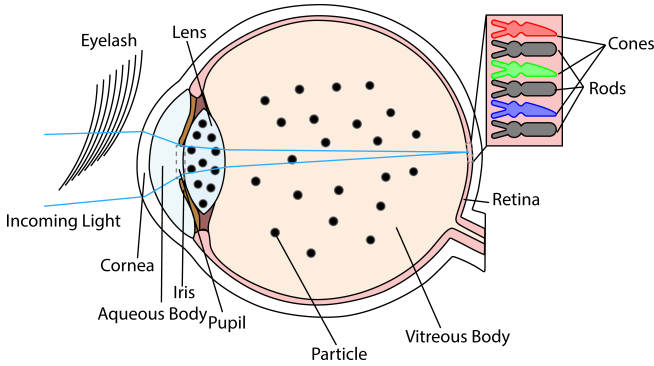
3 Physiological Background

Fig. 2. Sketch illustrating the anatomical structure of the eye. Incoming light reaches the retina often being refracted by the cornea and lens. It then stimulates the photoreceptor cells (cones and rods) on the retina. As light propagates toward the retina, its path may be affected by the presence of eyelashes, the iridal microstructure, and particles distributed on the lens and intravitreous body of the eyeball.

3.1 Optical Structure of the Human Eye

The eye components directly related to optical imaging and perception include the cornea, aqueous humour, iris (pupil), lens, vitreous body, and retina as shown in Fig. 2.

The function of the cornea and lens is to focus incoming light onto the retina. The iris can expand and contract to change the size of the pupil to control the amount of light entering the eye. The pupil diameter ranges approximately from 1.5 to 8 mm depending on the intensity of the surrounding light [Pamplona et al. 2009], which corresponds to a radius of 0.75 to 4 mm.

According to van den Berg et al. [2005], there are many evenly distributed particles in the cornea, lens, and vitreous body.

Table 1. A selected list of mathematical symbols that appear throughout multiple sections in this work.

Symbol	Description
$U(x, y, z)$	Complex amplitude at position (x, y, z)
$P(x, y)$	Pupil or obstacle at position (x, y)
j	Imaginary unit
λ	Wavelength (m)
k	Wave vector, $\|k\| = \frac{2\pi}{\lambda}$
(x_p, y_p, z_p)	Position on pupil plane
(x_i, y_i, z_i)	Position on image (retina) plane
d	Light propagation distance $(z_i - z_p)$ (m)
f	Focal distance (m)
a	Radius of a circular aperture (m)
$f/\#$	f-number of an optical system, $f/\# = \frac{f}{2a}$
$\mathcal{F}, \mathcal{F}^{-1}$	Fourier transform and its inverse
L_e	Radiance $(W \cdot sr^{-1} \cdot m^{-2})$
L_v	Luminance $(Nits)$
B	Brightness level

The retina contains two types of photoreceptor cells responsible for absorbing photons and generating signals: rods and cones [Grimes et al. 2018]. The cones are mainly responsible for daytime vision, while the rods are mainly responsible for nighttime vision.

3.2 Scalar Diffraction Theory

Geometric optics formulation is unsuitable for correctly handling the light propagation in the eyeball since the microstructures (*e.g.*, particles and fibers) in the eye can cause diffraction (wave optics) effects [Ritschel et al. 2009]. This section briefly introduces wave optics concepts required to properly account for those effects.

As an electromagnetic wave, light has two components: an electric field and a magnetic field. They are coupled through Maxwell's equations [Goodman 2017]. Following prior work [Luidolt et al. 2020; Ritschel et al. 2009], we assume that relevant ocular structures are much larger than the wavelength of light and adopt scalar diffraction theory, treating light oscillation as a scalar and neglecting polarization [Goodman 2017].

For brevity, we present only final formulas in the following sections. Readers interested in further details are referred to Section S1 of Supplementary Material. For convenience, Table 1 summarizes a selected list of mathematical symbols employed in this work.

3.2.1 Rayleigh-Sommerfeld Diffraction Theory. Under the scalar diffraction theory and finite aperture boundary conditions (*i.e.*, a finite aperture size), the Rayleigh-Sommerfeld (RS) diffraction solution provides an approximate monochromatic solution to Maxwell's equations, which can be expressed as [Goodman 2017]:

$$U(x_i, y_i, z_i) = \frac{z_i}{2\pi} \iint_P U(x_p, y_p, 0) \left(\frac{1}{r} - jk \right) \frac{e^{jkr}}{r^2} dx_p dy_p, \quad (1a)$$

$$r = \sqrt{z_i^2 + (x_i - x_p)^2 + (y_i - y_p)^2}, \quad (1b)$$

where $(x_p, y_p, 0)$ and (x_i, y_i, z_i) are points on the pupil plane and image plane, respectively, $U(x, y, z)$ is the complex amplitude that

encodes the amplitude and phase of a wave at a specific point, λ is the wavelength, $k = \frac{2\pi}{\lambda}$ is the wave vector and $P(x, y)$ is the mask representation of pupil or obstacle at position (x, y). We note that j is used to represent the imaginary unit.

The RS diffraction integral can be solved through convolution by defining u and v as:

$$u(x_p, y_p, z_p) = U(x_p, y_p, z_p), \tag{2a}$$

$$v(x_i, y_i, z_i) = \frac{z_i}{2\pi} \left(\frac{1}{r} - jk \right) \frac{e^{jkr}}{r^2}, r = \sqrt{z_i^2 + x_i^2 + y_i^2}, \tag{2b}$$

then the integral part of RS (Eq. 1) can be written as:

$$U(x_i, y_i, z_i) = \mathcal{F}^{-1}(\mathcal{F}(u)\mathcal{F}(v)), \tag{3}$$

where $\mathcal{F}, \mathcal{F}^{-1}$ are the Fourier transform and its inverse.

Although the convolution solution (Eq. 3) is accurate, it is computationally expensive. In practice, various diffraction approximations are commonly employed depending on the light propagation distance. In the remainder of this section, we briefly review the approximations relevant to our simulations.

3.2.2 Ochoa's Approximation.
Ochoa [2017] proposed that, for circular apertures, the RS diffraction solution (Eq. 1) can be approximated as:

$$U(x_i, y_i, z_i) = \frac{z_i}{2\pi} \mathcal{F} \left[U(x_p, y_p, 0) \left(\frac{1}{r_n} - jk \right) \frac{e^{jkr_n}}{r_n^2} \right] \left(\frac{x_i}{\lambda z_i}, \frac{y_i}{\lambda z_i} \right), \tag{4a}$$

$$r_n = \sqrt{x_p^2 + y_p^2 + z_i^2}. \tag{4b}$$

The error of this approximation decreases as the f-number ($f/\#$) increases [Ochoa 2017]. The f-number of an optical system is given by:

$$f/\# = \frac{f}{2a}, \tag{5}$$

where f and a respectively represent the focal length and the radius of the circular aperture causing diffraction.

3.2.3 Fresnel Approximation.
When the propagation distance z_i satisfies the condition:

$$z_i \gg \sqrt[3]{\frac{\pi}{4\lambda} [(x_i - x_p)^2 + (y_i - y_p)^2]_{max}^2}, \tag{6}$$

where max refers to the maximum possible expression value given any valid (x_i, y_i, x_p, y_p). Its corresponding approximation is named the Fresnel approximation and expressed as [Goodman 2017]:

$$U(x_i, y_i, z_i) = K\mathcal{F} \left[U(x_p, y_p, 0)e^{j\frac{k}{2z_i}(x_p^2 + y_p^2)} \right] \left(\frac{x_i}{\lambda z_i}, \frac{y_i}{\lambda z_i} \right),$$
$$K = \frac{e^{jkz_i}}{j\lambda z_i} e^{j\frac{k}{2z_i}(x_i^2 + y_i^2)}. \tag{7}$$

We note that the Fresnel approximation was adopted by Ritschel et al. [2009] and Luidolt et al. [2020] to reproduce glare.

3.2.4 Chirp Z Transform.
The computation of Fourier transforms can be more efficiently carried out using the Fast Fourier transform (FFT) [Goodman 2017]. A generalized version of the FFT, called Chirp Z transform (CZT) [Bluestein 1970], allows for more flexibility in the selection of a region of interest in frequency space [Hu et al. 2020]. Accordingly, one can directly generate the pattern on the image plane within the region of interest without having to scale it or crop it afterwards (Section 6.6).

3.3 Visual Adaptation

In addition to diffraction, visual adaptation is also relevant to the perception of the glare phenomenon. We review relevant cone and rod properties included in our model.

3.3.1 Cones and Rods.
There are three types of cones—L, M, and S—that are sensitive to long, medium, and short wavelengths in the visible spectrum, respectively [Banterle et al. 2018]. There is only one type of rod, however. Therefore, the cones are directly associated with the perception of color (chromatic vision), while the rods are not (achromatic vision) [Ferwerda et al. 1996]. Color spaces, such as LMS, were developed taking these aspects into consideration [Banterle et al. 2018].

3.3.2 High Dynamic Range.
Cones and rods collaborate to provide humans with vision across a dynamic range that can be divided into scotopic level (10^{-6} to 10^{-2} Nits), mesopic level (10^{-2} to 10^{1} Nits), and photopic level (10^{1} to 10^{8} Nits). Rods are quite sensitive to light and provide achromatic vision at the scotopic level of illumination. Cones are less sensitive than rods, providing chromatic vision at the photopic level of illumination. Both types of cells contribute to vision under mesopic illumination [Grimes et al. 2018].

3.3.3 Non-linear Perception and Stimulus Threshold.
Human vision follows Weber-Fechner's law [Banterle et al. 2011]. It states that an additional physical stimulus (*e.g.*, light) needs to surpass a certain threshold to make humans notice the existence of the additional stimulus (increment in brightness), and such a threshold is proportional to the logarithm of the existing stimulus [Banterle et al. 2011]. Ferwerda et al. [1996] investigated the relationship between this threshold and background luminance (Fig. 3) and approximated the curve as:

$$\log t_p = \begin{cases} -0.72, & \text{if } \log L_v \le -2.6, \\ \log L_v - 1.255, & \text{if } \log L_v \ge 1.9, \\ (0.249 \log L_v + 0.65)^{2.7} - 0.72, & \text{otherwise.} \end{cases} \tag{8}$$

$$\log t_s = \begin{cases} -2.86, & \text{if } \log L_v \le -3.94, \\ \log L_v - 0.395, & \text{if } \log L_v \ge -1.44, \\ (0.405 \log L_v + 1.6)^{2.18} - 2.86, & \text{otherwise.} \end{cases} \tag{9}$$

where L_v is the background luminance and t_p, t_s are thresholds for cones and rods, respectively. Those two curves (Eqs. 8 and 9) are henceforth referred to as threshold versus intensity (TVI).

3.3.4 Photo-sensitivity and Bleaching.
The sensitivities of cones and rods are strongly affected by rapid changes in the illumination of an environment. According to Ferwerda et al. [1996], when the environment suddenly becomes bright, rods restore 80% of their
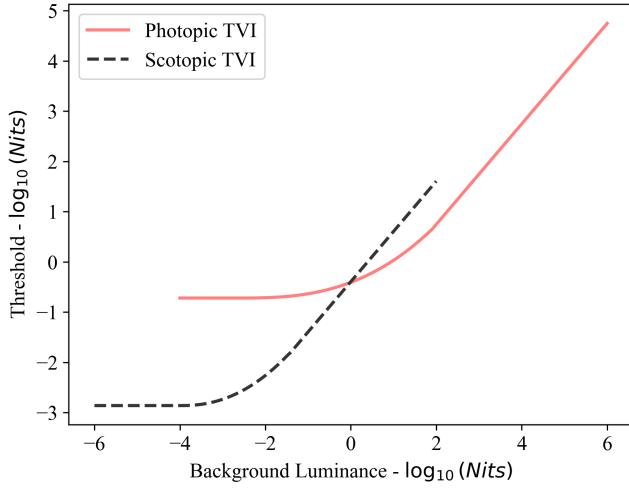
Fig. 3. Graph depicting TVI values as a function of background luminance [Ferwerda et al. 1996]. It indicates the minimum luminance difference that must be exceeded for a person to perceive a change in brightness against a given background luminance.
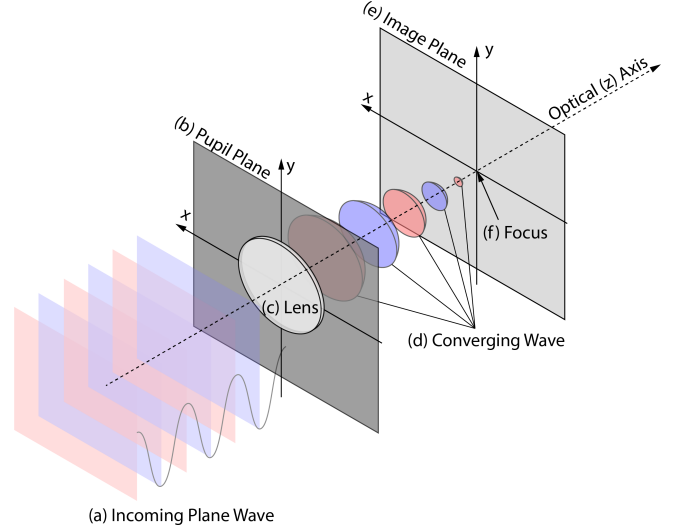

Fig. 4. Sketch illustrating the main steps of wave propagation modeling employed in this work. The incoming plane wave (a) is converged (d) by the focus lens (c) on the pupil plane (b). It then propagates to the focus (f) on the image plane (e).

photo-sensitivity in two seconds, while it takes 10 minutes for the cones to fully restore their sensitivity. Besides, rods lose their effectiveness in very bright conditions, a phenomenon called bleaching [Ferwerda et al. 1996].

We note that the HVS is much more complex than the concise description provided in this section. In fact, the coordination mechanism between cones and rods in the mesopic level of illumination is still not completely understood [Grimes et al. 2018].

4 Proposed Framework

We simulate the glare phenomenon by decomposing its eliciting process into two stages, namely, propagation and response. The setup and simulation process are schematically illustrated in Figs. 4 and 5, respectively.

In the propagation stage, we model how the light enters the eyeball and induces a stimulus on the retina with a glare pattern that is quantitatively described by the PSF [Kakimoto et al. 2004; Ritschel et al. 2009], which we expand on by employing the wave propagation methods mentioned in Section 3.2.1 and Section 3.2.2.

In the response stage, we model how the stimulus from light is processed by the photoreceptor cells. We propose a physiologically-inspired algorithm that converts the radiance field on the retina into a tristimulus brightness level. The algorithm accounts for the specific characteristics of the HVS introduced in Section 3.3.

4.1 Simulation Setup

The propagation stage includes the modeling of the light source, lens, pupil, obstacles, and retina. In the context of wave optics, the light wave on the pupil plane (i.e., the light emitted by the source that reaches the pupil plane) is represented by its complex amplitude. The lens is then represented by a phase transformation that modifies the phase of this wave [Goodman 2017] as represented in Fig. 4.

Additionally, pupils and obstacles are represented as masks on the pupil plane. The light wave on the image plane is also represented by its complex amplitude, and it is expected to be computed based on the propagation of light waves from the pupil plane.

Aligned with previous works [Kakimoto et al. 2004; Ritschel et al. 2009], we set the lens at the origin, with the z-axis as the optics axis. We also set the retina plane to be $z = d$, where d is the propagation distance. The light source is a plane wave (i.e., directional light) parallel to the eye axis, and the lens can achieve perfect focus (i.e., $d = f$ where f is focal length). With the above setting, we can define the light source and perfect focus lens using the following expressions:

$$U_0(x_p, y_p, 0) = A \cdot e^{-j \cdot k \cdot z_p}, \tag{10a}$$

$$t_{lens}(x, y) = e^{-j \frac{k}{2f}(x^2 + y^2)}, \tag{10b}$$

where U_0 is the wave field induced by the light source, t_{lens} is the phase transformation from the lens, and A is the amplitude of a wave. The incident wave field (U) is then expressed as

$$U(x_p, y_p, 0) = U_0(x_p, y_p, 0) \times P(x_p, y_p) \times t_{lens}(x_p, y_p). \tag{11}$$

Based on anatomical data [Atchison and Thibos 2016], and for simplicity, we set the distance from the center of the lens to the retina to be 20 mm and the refractive index of the liquid in the eyeball to be 1.4.

4.2 Propagation Stage

Considering the setup schematically presented in Fig. 4, we can calculate the light wave (represented by complex amplitude) at the retina (image plane) by applying any of the propagation methods introduced in Section 3.2 to the light wave on the pupil plane: RS
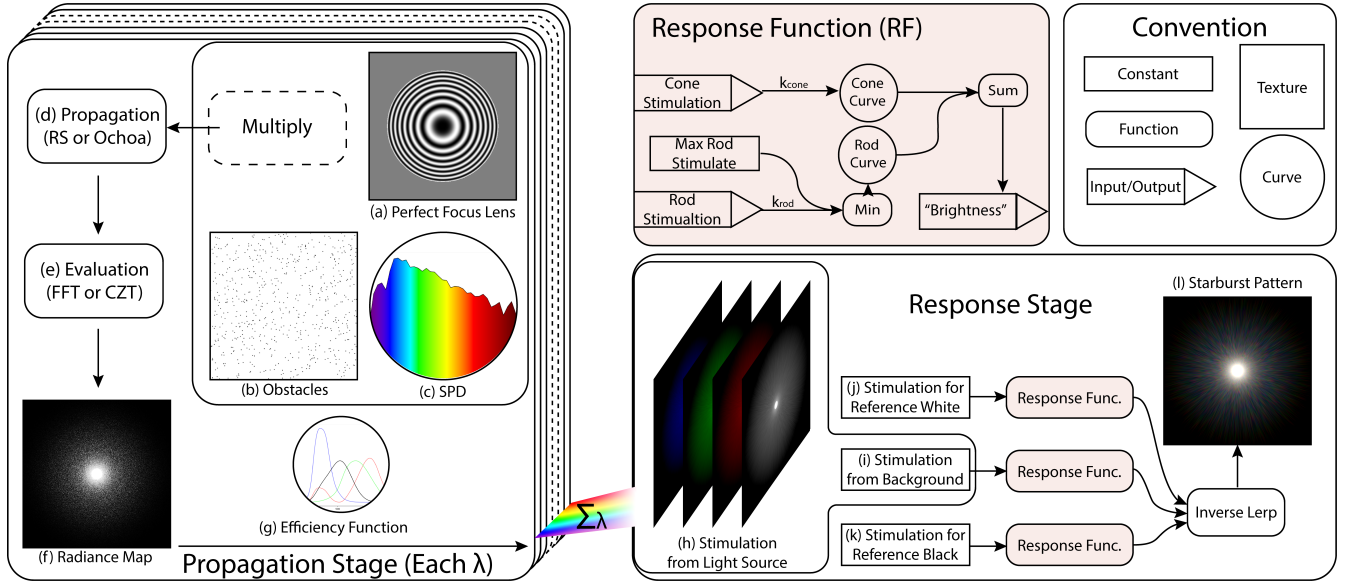
Fig. 5. Overview of the framework proposed for the plausible reproduction of the glare patterns. A parallel incoming light, represented by its spectral power distribution (c), passes through a perfect focus lens (a) and an obstacle mask (b). The resulting wave field is computed using wave propagation methods (d), implemented numerically (e). The propagation results on the retina are converted to a radiance map (f) and further converted into luminance by weighting by the spectral luminous efficiency. The propagation stage is evaluated once for each wavelength, and the results are accumulated to obtain the stimulus (h) on the retina from the light source. The response function is applied to the sum of the stimulus and background luminance (i) to compute brightness. The final result (l) is obtained by applying inverse linear interpolation (Lerp) between the brightness levels of reference black (k) and reference white (j).

diffraction (Eq. 1), Ochoa's approximation of RS (Eq. 4), and Fresnel approximation (Eq. 7).

4.2.1 Visual Resolution Improvement. Besides increasing physical accuracy, we aim to improve the visual resolution of the simulation results (generated image or PSF). We achieve that by implementing the Fourier Transform using CZT (Section 6.3). We remark that CZT enables users to manually select the region they are interested in.

4.2.2 Complex Amplitude to Radiance Conversion. Recall that radiance (L_e) corresponds to irradiance per solid angle [Glassner 2004]. The complex amplitude ($U(x, y, z)$) at the image plane needs to be converted to radiance to support rendering calculations. We know that irradiance is proportional to the magnitude of complex amplitude [Goodman 2017]. We also assume that the solid angle connecting the points on the lens and the pixels has approximately the same magnitude, *i.e.*, any small difference can be considered negligible. Accordingly, we employ the following conversion expression:

$$L_e = c_u |U|^2, \tag{12}$$

where the constant c_u is a user-defined parameter based on the choice of light source intensity (*e.g.*, bright or dim).

4.3 Response Stage

The stimulus that the light wave induces on the retina is not directly equivalent to what humans perceive. We believe that background luminance should be regarded as an essential component of the glare phenomenon. As pointed out by Mainster and Turner [2012], the reduction of contrast caused by the glare phenomenon is more

significant when the ratio between the light source luminance and the background luminance is larger. In other words, glare can be more easily perceived in dim backgrounds than in brighter ones. We also remark that humans tend to ignore the details (specifically, contrast arising from subtle luminance variations) if the stimulus does not surpass the stimulus threshold as discussed in Section 3.3.3. Hence, we concluded that the response stage of the algorithm should allow some portions of the pattern to dissolve into the background since their luminous intensity may not reach the threshold (Section 3.3.3) required to enable their perception by human observers. Accordingly, we elected to develop a novel response function based on the observations and the measurements conducted by Ferwerda et al. [1996].

4.3.1 Radiance to Luminance Mapping. After we calculate the radiance distribution (L_e) of the image plane (Section 4.2.2), we multiply it by the spectral power distribution ($M_{rel}(\lambda)$), spectral luminous efficiency ($V(\lambda)$ and $V'(\lambda)$), and integrate over all visible wavelengths to compute the photopic luminance:

$$L_v^{photopic} = \int_{360\ nm}^{830\ nm} V(\lambda) M_{rel}(\lambda) L_e(\lambda) d\lambda, \tag{13}$$

and the scotopic luminance:

$$L_v^{scotopic} = \int_{360\ nm}^{830\ nm} V'(\lambda) M_{rel}(\lambda) L_e(\lambda) d\lambda, \tag{14}$$

where $V(\lambda)$ and $V'(\lambda)$ are photopic and scotopic spectral luminous efficiencies, respectively.

4.3.2 Luminance to Brightness Mapping. We build our mapping algorithm using the threshold versus intensity (TVI) curve (Fig. 3), which indicates the minimum stimulus required for a brightness increase to be perceived. Assuming that each perceived increment in brightness is treated identically across different base luminance levels, the required stimulus (threshold of perception) at any given brightness level B can be calculated iteratively as:

$$L_v(B = 0) = 0; \tag{15a}$$

$$L_v(B = i + 1) - L_v(B = i) = TVI(L_v(B = i)). \tag{15b}$$

Eq. 15a represents the trivial base case in which the absence of illumination simply corresponds to zero brightness, and vice versa. Eq. 15b conveys that the amount of luminance needed to increment brightness level i by one is given by the TVI curve evaluated at luminance with brightness level i which is $TVI(L_v(B = i))$. Since Eq. 15 is monotonically increasing, we could use its inverse function (L_v^{-1}) to build a mapping from luminance to brightness.

To simulate the bleaching effect of rods (Section 3.3.4), we set the upper bound of stimulus from rods to 10 Nits [Ferwerda et al. 1996]. For the adaptation effect (Section 3.3.4), sensitivities, as user-defined parameters, are introduced as coefficients to the cone stimulus and rod stimulus, respectively. Lastly, the brightness level calculated from both cones and rods is combined and expressed as:

$$B(L_v^p, L_v^s) = B^p(k_{cone} \cdot L_v^p) + B^s(\min(k_{rod} \cdot L_v^s, 10)), \tag{16}$$

where B^p and B^s are the inverses of Eq. 15, obtained by substituting the photopic and scotopic TVI into the equation, respectively. Recall that cones are associated with photopic illumination, while rods are associated with scotopic illumination (Section 3.3.1). Accordingly, L_v^p and L_v^s respectively correspond to stimuli (expressed in terms of luminance) applied to these photoreceptor cells, with k_{cone} and k_{rod} representing their sensitivities (required for the simulation of the adaptation effect).

For the implementation of B^p and B^s, we fit the discrete results of Eq.15 using the analytical form given in Eq.S20. Further details can be found in Supplementary Material Section S3.

4.4 Background Luminance and Displaying Parameters

In addition to the light source, the background luminance also needs to be accounted for, and it is introduced by simply adding a new parameter L_v^{env} to the stimulus. L_v^{env} can be computed by radiance or luminance rendering using renderers such as Mitsuba [Nimier-David et al. 2019].

After mapping luminance to brightness using Eq. 16, the resulting brightness levels may still be outside the 0 to 255 range used for pixel color values. To address this, we manually define the stimulus corresponding to black and white points as $L_v^{refBlack}$ and $L_v^{refWhite}$ (denoted in the equation as rB and rW due to space constraints), respectively. The resulting LMS color components are calculated by applying inverse linear interpolation (Lerp) and taking the combined brightness of the pattern and environment, the brightness of the reference black, and the brightness of the reference white as input

values. This is accomplished using the following equation:

$$c_{LMS}[i] = \frac{B(L_v^p[i] + L_v^{env}[i], L_v^s[i] + L_v^{env}[i]) - B(rB[i], rB[i])}{B(rW[i], rW[i]) - B(rB[i], rB[i])}, \tag{17}$$

where LMS is the color space that represents the response of three types of cones [Banterle et al. 2018], with $i = \{1, 2, 3\}$ representing each color component. For the derivation of Eq. 17, please refer to Supplementary Material Section S2. The final color in RGB space is then obtained by multiplying the LMS color values with the transform matrix M_{RGB}^{LMS} [Banterle et al. 2018]:

$$c_{RGB} = M_{RGB}^{LMS} \times c_{LMS}. \tag{18}$$

5 Implementation

We implement each approximation algorithm with NumPy and Diffractio [Sanchez-Brea et al. 2024] library, which provides routines that implement the RS diffraction with convolution and CZT. To facilitate visual interaction, we implement the response stage in a fragment shader with OpenGL [Kessenich et al. 2017] and adopt Dear ImGui [Cornut 2024] as the user interface. Simulations are executed on a workstation with 128 GB RAM equipped with an AMD Ryzen 3990X. For more details, please refer to Supplementary Material Section S3. For reproducibility purposes, we release the code for glare pattern generation and simulation, allowing researchers to reproduce and extend our results [Sun and Baranoski 2025].

6 Propagation Aspects

In Section 3, we introduced the RS diffraction theory as the solution for propagation under scalar diffraction theory, and mentioned its suitability for light propagation in the eyeball. In this section, each approximation method used in the propagation stage will be theoretically assessed by comparing its PSF to that provided by the RS solution.

6.1 Scene and Baseline

Under the eyeball scenario, we analyze each method by assigning:

- wavelength: $\lambda = 360\ nm, \eta = 1.4$,
- size of plane: $\rho = (x_i - x_p)_{max} = (y_i - y_p)_{max} = 8\ mm$,
- propagation distance (also focal length): $z = f = 20\ mm$, and
- pupil radius: $a_{day} = 1\ mm, a_{night} = 3\ mm$.

Note that, although RS meets the theoretical conditions (Section 3.2), a reliable assessment still requires the sampling density to meet the Nyquist limit, which corresponds to the smallest sampling density required to completely recover a signal [Goodman 2017]. The required sampling interval is given by [Shen and Wang 2006]:

$$\Delta\rho = \sqrt{\lambda^2 + \rho^2 + 2\lambda\sqrt{\rho^2 + d^2}} - \rho. \tag{19}$$

Considering the values assigned to λ, η, ρ and $d = f$, the size ($N \times N$) of the square matrix representing the pupil plane needs to be at least $\rho/(\Delta\rho)$, which yields 11555 in this case (rounds up to 16384 for FFT). Given this relatively large matrix size, a suitable approximation is necessary to manage potential computational costs.

6.2 Theoretical Soundness

In this subsection, we assess the theoretical soundness of each propagation approximation considered in this work. Although the failure to meet the conditions for an approximation suggests that the propagation result may be physically inaccurate, it may still lead to visual outcomes with a quality level suitable for computer graphics applications centred on the rendering of believable images [Greenberg et al. 1997].

6.2.1 Ochoa's approximation. According to Ochoa's experiments, the relative error of the approximation decreases monotonically as the f-number ($f/\#$) of the optical system increases. In the eyeball setting, the lower bound of f-number is $f/\# = \frac{20\ mm}{7mm} = 2.86$. Since the relative error with $f/\# = 2$ is already below 2% in Ochoa's results, the error in our case should be even smaller. Therefore, applying Ochoa's approximation is expected to introduce a relative error less than 2%.

6.2.2 Fresnel approximation. The distance requirement for the Fresnel approximation can be directly calculated from Eq. 6, and substituting the selected values results in a required propagation distance far greater than 323.5 *mm*. However, the distance from the lens to the retina is only around 20 *mm*, which is much shorter than required. Thus, in theory, Fresnel diffraction cannot fully account for wave propagation in the eyeball. Nevertheless, as indicated by Ritschel et al. [2009], it can still be employed to produce believable patterns that can make computer-generated scenes appear brighter.

6.3 Airy Disk from Each Propagation Method

Single wavelength propagation with an ideal focus lens should produce an Airy disk [Goodman 2017]. We will assess the combination of each approximation of propagation with the selected λ, ρ, z and f values mentioned in Section 6.1. For effective comparison, each pattern's energy is shifted to ensure that the centre intensities are the same for all patterns shown in this and the next subsection.

Figs. 6a, 6b, and 6c presents images of Airy disks generated considering a 1 *mm* pupil radius using the RS diffraction solution (Fig. 6a), Ochoa's approximation (Fig. 6b), and Fresnel approximation (Fig. 6c), respectively. Overall, these images are similar. They show that Ochoa's approximation (proposed in this work) and Fresnel approximation (adopted by previous works [Luidolt et al. 2020; Ritschel et al. 2009]) are effective for handling the propagation in the 1 *mm* pupil radius case. However, the previous statement does not hold when a large (3 *mm*) pupil radius is considered. Airy disks shown in Figs. 6d, 6e, and 6f were generated using the same propagation methods as Figs. 6a, 6b, and 6c, respectively, but considering a 3 *mm* pupil radius. The image obtained using the Fresnel approximation (Fig. 6f) differs considerably from the image obtained using the RS diffraction solution (Fig. 6d). On the other hand, the image obtained using Ochoa's approximation (Fig. 6e) closely approximates the reference RS image (Fig. 6d). These observations indicated that the Fresnel approximation (adopted by previous works [Luidolt et al. 2020; Ritschel et al. 2009]) may significantly underestimate the extent of the pattern for a relatively larger pupil radius.
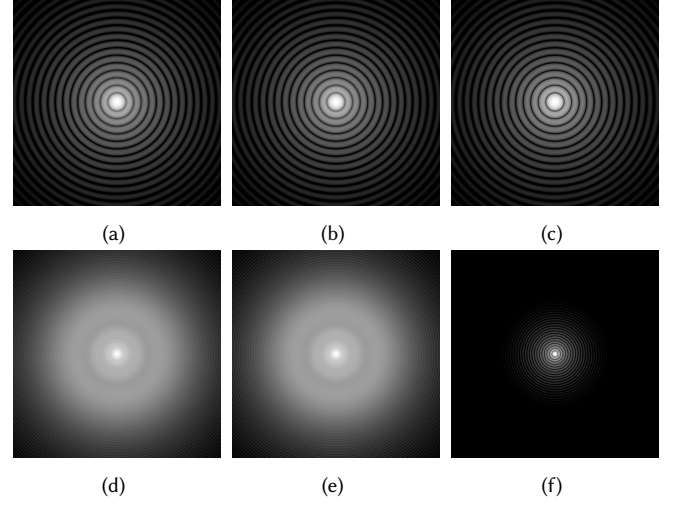
Fig. 6. Airy disks generated using different propagation methods and considering different pupil radii. Left column: RS diffraction. Middle column: Ochoa's approximation. Right column: Fresnel approximation. Top row: 1 *mm* radius. Bottom row: 3 *mm* radius.
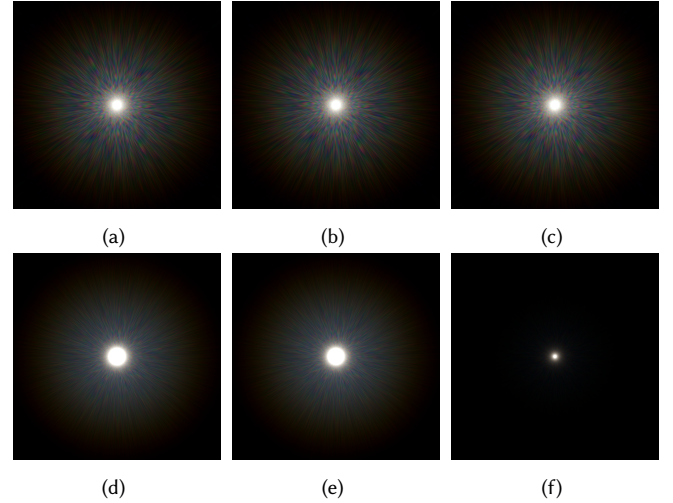

Fig. 7. Glare patterns generated using different propagation methods and considering different pupil radii. Left column: RS diffraction. Middle column: Ochoa's approximation. Right column: Fresnel approximation. Top row: 1 *mm* radius. Bottom row: 3 *mm* radius.

6.4 Glare Pattern from Propagation Method

The previous section presented the Airy disks generated using different propagation methods and considering different pupil radii. In this section, we present results obtained considering obstacles, specifically particles, added to the lens as a mask. Glare patterns depicted in Figs. 7a, 7b, and 7c were generated using the RS diffraction solution, Ochoa's approximation, and Fresnel approximation, respectively. As can be observed by inspecting these results, the

differences among the patterns generated using these different propagation methods were visually negligible when we considered a 1 *mm* pupil radius. Glare patterns shown in Figs. 7d, 7e, and 7f were generated using the same propagation methods as Figs. 7a, 7b, and 7c, respectively, but considering a 3 *mm* pupil radius. It can be observed that the pattern generated using the Fresnel approximation (Fig. 7f) significantly underestimated the extent of the pattern for a relatively larger pupil radius. Nevertheless, one can still obtain a pattern that is suitable for computer graphics applications by increasing the intensity of the pattern at the cost of overexposing its central area.

6.5 The Decay of the Energy in the Patterns

The dynamic range of the glare pattern is relatively large. We compute the extent of the patterns in Fig. 7 by taking the average of the logarithm of the Y channel of the cone stimulus on the circle with distance r to the focus point o as shown in the following expression:

$$f(r) = \frac{1}{2\pi r} \int_{|x-o|=r} \log_{10}(L_v(x))dx. \tag{20}$$

Note that we manually shift the max of each curve to zero to compare the decay rate effectively. The results presented in Fig. 8 show that the energy of the pattern decreases quickly along the radial direction as the energy is reduced by around five orders of magnitude when the distance is at 125 *μm* to the center. Meanwhile, we can quantitatively observe that the Fresnel approximation significantly underestimates the energy of the pattern when the pupil radius is large as discussed in the last section.
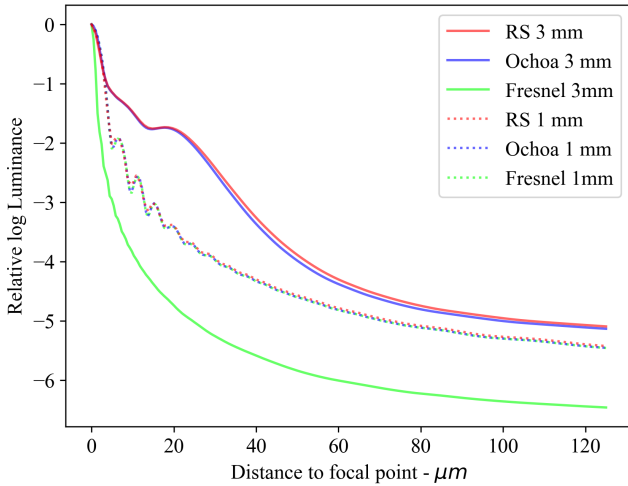

Fig. 8. Relative average log luminance vs. distance plot for glare patterns depicted in Fig. 7, computed using Eq. 20.

6.6 Reducing Error using Chirp Z Transform

A factor affecting the visual quality of the patterns is the physical size of the image plane, which corresponds to the number of pixels within the region of interest. Although the size $(N \times N)$ of the matrix
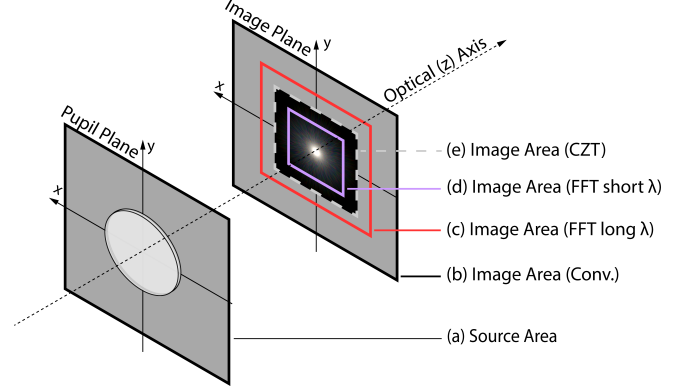

Fig. 9. Diagram showing the variation in the physical size (in $\mu m \times \mu m$) of the square matrix $(N \times N)$ used to represent the complex amplitude of the light wave on the pupil (image) plane. (a) Physical area on the pupil plane that corresponds to the matrix. (b) Physical area on the image plane after the propagation implemented with convolution. (c) Physical area on the image plane after the propagation of waves using an FFT implementation for long wavelengths. (d) Physical area on the image plane after the propagation using an FFT implementation for short wavelengths. (e) Physical area on the image plane after the propagation using CZT implementation.

that represents the light wave stays constant during the propagation stage, its corresponding physical size (in $\mu m \times \mu m$) may change as shown in Fig. 9.

Such a variation in physical size can occur during the propagation stage implemented using different methods. With the convolution implementation (Section 3.2.1) of the RS diffraction solution, the physical size of the resulting matrix is always the same as the source matrix, regardless of the wavelength at which the light is being propagated [Claus and Rodenburg 2015]. However, this condition does not hold if FFT is directly applied to the pupil plane since the physical size of the resulting image plane is proportional to the wavelength [Goodman 2017]. This difference can be traced back to the formulations of the diffraction solutions. In the convolution implementation (Eqs. 2 and 3), the input coordinates are x_i and y_i, whereas in the implementation where FFT is directly applied to the pupil plane (Eqs. 4 and 7), the input coordinates are divided by the wavelength and propagation distances, resulting in $x_i/(\lambda z)$ and $y_i/(\lambda z)$.

The aforementioned change in physical size leads to the requirement of further scaling of the image plane so that the generated matrix can have the same physical size for all wavelengths (or resampling equivalently [Luidolt et al. 2020; Ritschel et al. 2009]). Moreover, the area of interest may only occupy a small portion of the resulting matrix. These limitations induce extra computational costs and possibly introduce errors during resampling. In comparison, CZT solves this problem as it allows users to select the region of interest (physical size of image plane) [Hu et al. 2020]. This feature, in turn, also enables the selection of the same physical size for all wavelengths, thus inherently addressing the size variation issue without the need for resampling.

Fig. 10 presents the results obtained for a 1 *mm* pupil radius using the Fresnel approximation and the FFT and CZT implementation

methods. Overall, the results appear similar as expected, albeit the pattern obtained using FFT (Fig. 10a) is more blurred. Also, some aliasing can be observed between the rings of the patterns obtained using FFT (Fig. 10a, insets).
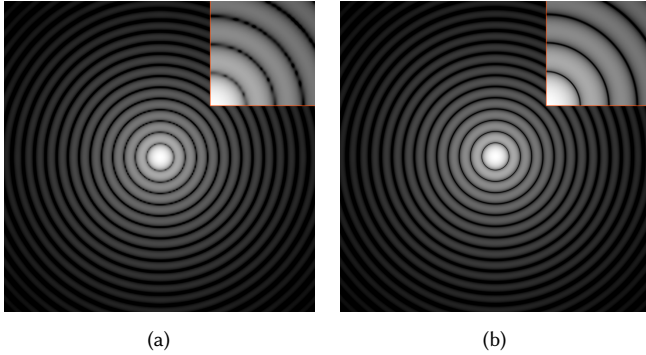

(a)   (b)

Fig. 10. Airy patterns generated for a 1 *mm* pupil radius using Fresnel approximation and different implementation methods. (a) Present pattern generated using FFT. (b) Present pattern generated using CZT. The insets in the top-right corners of each subfigure provide a zoom-in view of the central region.

Overall, the advantages discussed above originate from the fundamental difference in the sampling process: in the direct FFT implementation, the continuous diffraction formula is sampled first and then rescaled, whereas in CZT, the continuous diffraction formula is scaled first and then sampled (without further rescaling needed). This order of operations allows CZT to achieve consistent physical sizing and significantly reduce aliasing artifacts.

6.7 Time and Space Efficiency

All propagation methods introduced in Section 3.2 and CZT were implemented using a constant number of FFT operations and their inverses. Although these methods share the same time complexity $O(N^2 log N)$, Ochoa's approximation is approximately 6× faster than the reference RS solution, whereas the Fresnel approximation is only about 3× faster. It is worth noting that Ochoa's approximation produces results closer to the reference patterns (obtained using the RS diffraction solution) than those of the Fresnel approximation. For these reasons, we suggest the use of Ochoa's approximation, instead of the Fresnel approximation, in the generation of the glare patterns discussed in this work.

Note that the computation of the PSF for the glare pattern is performed offline and does not impact runtime performance. For this reason, we do not elaborate on it further. The reader interested in more details is referred to Supplementary Material Section S4.

7 Practical Ramifications

For the propagation stage, we assessed the generated glare patterns (described by the PSF) by comparing them with the baseline patterns generated using the RS diffraction solution. However, we are not able to quantitatively evaluate the results obtained through the response stage (Section 4.3) since, to the best of our knowledge, there is no current technology capable of capturing the exact glare

pattern as seen by human observers. Please refer to Supplementary Material Section S5 for examples illustrating the limitations of camera imaging systems with respect to the photographic capture of glare patterns. Hence, we elected to qualitatively examine the visual simulation results obtained for different illumination conditions. We note that all patterns depicted in this section were generated using Ochoa's approximation (Section 3.2.2) and CZT implementation (Section 3.2.4).

7.1 The Role of Background Luminance

Previous works usually pay attention to the light source and overlook the background luminance around the light source. The results presented in Fig. 11 show that as the background luminance increases, the pattern generated by a light source gradually disappears. In Fig. 12, we set the reference black equal to the background luminance so that we can extract the pure glare patterns depicted in Fig. 11. Therefore, to make a glare pattern noticeable, the intensity of the light source should be significantly greater than the background illumination. Such a behaviour could be attributed to both the luminance distribution of the pattern (PSF) and the perception threshold (Section 3.3.3). Inspecting the curves depicted in Fig. 8, one can notice that the luminance drops exponentially as the distance from the center increases.

Moreover, as discussed in Section 3.3.3, the perception threshold requires a certain amount of additional stimulus from the pattern so that the patterns can appear to human observers. Human observers can see a pattern only if the light source is bright enough. This can happen when the energy associated with the outer part of a spike in the PSF, which has much smaller energy than the center, can induce sufficient stimulus to surpass the perception threshold for a given background.

7.2 The Effect of Overall Luminance

The previous section addressed relative luminance requirements for the glare pattern to be noticeable. It is important to note, however, that the absolute luminance and the state of photoreceptor cells (*i.e.,* photo-sensitivity) also affect the visual appearance of the pattern. We remark that, for scenes with a relatively high illumination intensity, the cone responses are dominant, while for scenes with relatively low illumination intensity, the rod responses are dominant (Section 3.3.2).

We selected four cases to illustrate this aspect. Fig. 13a depicts relatively high-intensity light from both the light source and the background illumination. Since cones have a dominant role in this case, the resulting pattern is colorful. Fig. 13b, which depicts a rod-dominated case, has an opposite illumination setting of Fig. 13a, resulting in a pattern with an achromatic appearance. Fig. 13c depicts an illumination arrangement intermediate between the two previous cases. Lastly, Fig. 13d depicts a case in which the light source appears suddenly (*e.g.*, when a car makes a sharp turn in a corner and enters an observer's field of view). In this situation, the observer's rods are saturated and the cones are at a lower sensitivity state.
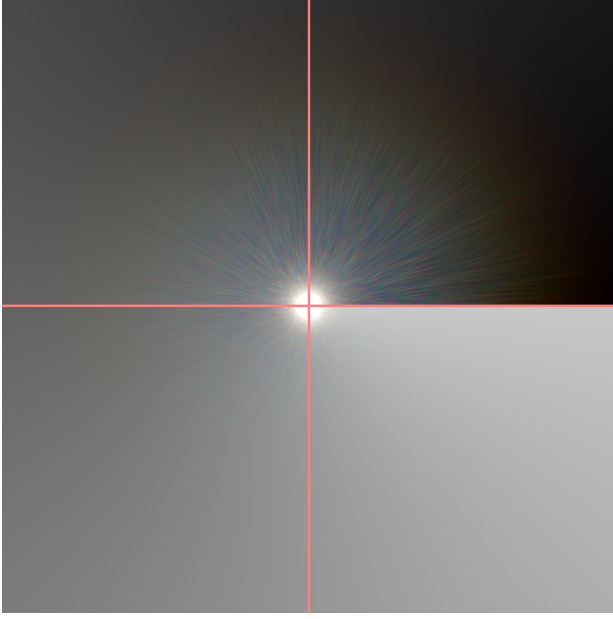
Fig. 11. A sequence of images illustrating the effects of background luminance variation. As the luminance of the background light increases from the first quadrant (top right) going counter-clockwise, the pattern begins to dissolve into the background. The rationale is that the threshold for incremental brightness level is increasing as the background luminance increases, thus the noticeable pattern shrinks as the background luminance increases.
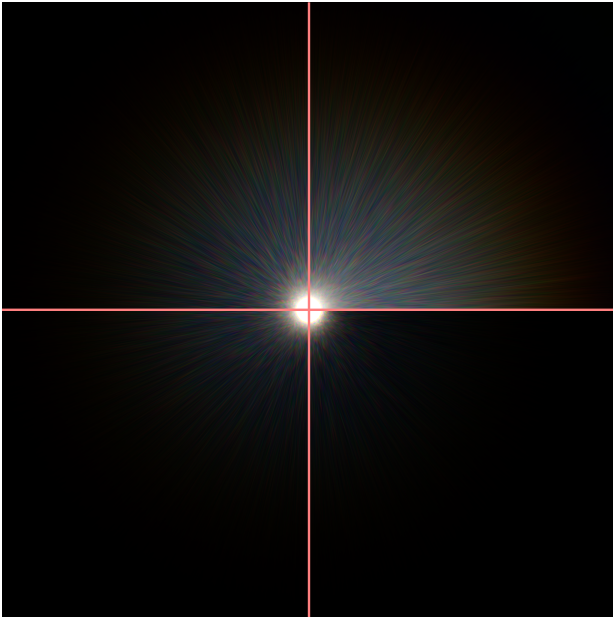

Fig. 12. A sequence of images illustrating respectively pure versions of the glare patterns depicted in Fig. 11. Images were obtained by setting the reference black to the luminance of the background.
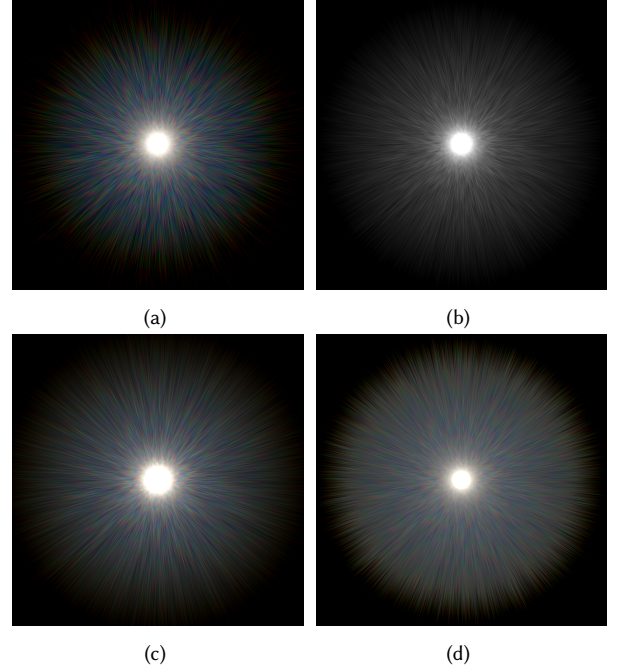

(a)   (b)

(c)   (d)

Fig. 13. Images showing a glare pattern under different illumination conditions. (a) Depicts a scene with high light source and background intensities. (b) Depicts a scene with low light source and background intensities. (c) Presents the result of mixing (a) and (b). (d) Depicts the scene with rod saturation and low cone sensitivity.

7.3 Rendering Applications

We render two distinct scenes[1] (presented in Figs. 14 and 15) to illustrate the plausible depiction of the glare phenomenon in different scenarios as well as the visual enhancements brought about by the proposed visual response function (Section 4.3). The patterns are incorporated into the scenes by directly placing them around the light sources before applying the response function.

As mentioned in Section 1, driving is a classic scenario for human observers to see the glare patterns. Fig. 14 depicts examples that can be seen at spots where the specular reflection of sunlight takes place during daytime. Fig. 15, on the other hand, depicts examples of the patterns that can be seen around car headlights at night. We note that patterns in the daytime scene and nighttime scene were generated considering 1 *mm* and 3 *mm* pupil radii, respectively.

For the daytime scenes, we can observe that the patterns' visibility is affected by the local background luminance as depicted in Fig. 14. More specifically, the patterns are more noticeable around the darker regions (*e.g.*, indoors, car tires, and car interiors) and less noticeable around the brighter regions (*e.g.*, the sky and body of the car).

Turning to the nighttime scene, by considering a mixed illumination setting, with both cones and rods providing considerable contributions (*e.g.*, as illustrated in Fig. 13c), the patterns generated using our proposed response function, presented in Fig. 15, show a low-saturation color and a fade-out transition into the background.

[1]Assets: "Barcelona Pavillion" (eMirage, CC BY) and "Car Demo" (Mike Pan, CC0).

We can observe that the scene depicted in Fig. 15 looks less colorful than the one depicted in Fig. 14. This may be attributed to the role played by the rod cells [Pattanaik et al. 1998], which are activated in low-illuminated environment. In addition, the pattern spikes in the nighttime scene are denser than those in the daytime scene due to the dilation of the pupil.

It is worth highlighting that the overall visual depiction of glare patterns results from multiple factors, including the scene illumination level and the distinct photoreceptor sensitivities, with the rods taking seconds to restore their sensitivity instead of minutes taken by the cones (Section 3.3.4). We remark that each person may see different patterns due to the eye structure diversity. Accordingly, besides typical graphics applications, the proposed framework might allow individuals to assess their own perception of glare patterns through the modification of simulation parameters.

7.4 Discussion and Limitation

The proposed response function offers a possible explanation for why the pattern appears only near bright light sources (Section 7.1). It also accounts for the difference in perceived appearance between daytime and nighttime conditions (Section 7.2). However, due to the nature of the glare phenomenon, this explanation cannot be formally validated like the methods employed in the propagation stage. Nevertheless, we regard this as a meaningful aspect since it highlights perceptual implications that merit further study and contribute to improved visual quality in practice.

We note that the proposed visual response function and tone mapping operators share the same domain and range, as both of them map the physical value on the retina to the display. However, we did not adopt existing tone mapping algorithms since their design goals emphasize detail preservation, whereas our objective is to allow details below perceptual thresholds to dissolve into the background.

8 Conclusion

This work described a framework proposed for the plausible reproduction of glare patterns. Compared to previous works, it is capable of generating patterns with higher physical fidelity and resolution. By considering specific characteristics of the human visual system and background luminance, the proposed framework can be employed to generate plausible depictions of glare patterns for distinct illumination scenarios.

We employed the Rayleigh-Sommerfeld diffraction solution and its Ochoa's approximation. To the best of our knowledge, these algorithms have not been used in similar computer graphics applications before. They are capable of enhancing the physical correctness compared to Fresnel and Fraunhofer approximations adopted in previous works [Kakimoto et al. 2004; Luidolt et al. 2020; Ritschel et al. 2009]. In addition, replacing the Fast Fourier transform by the Chirp Z transform in the implementation of these approximations allows for a further increase in the visual resolution of the generated patterns. We also proposed a novel physiologically-inspired algorithm that approximates the visual adaptation human visual system. It is based on measured data from Ferwerda et al. [1996], and

it incorporates factors such as rod contribution, visual thresholds, and photoreceptor sensitivities.

As future work, we intend to consider other biological structures (*e.g.*, eyelash and lens grating) that may also affect the diffraction of light reaching the retina [Ritschel et al. 2009]. Furthermore, we plan to explore the use of the vector diffraction theory [Goodman 2017] to increase the physical correctness of our simulations by properly accounting for eye microstructures (*e.g.*, particles) that have a size (less than 10 μm [Simpson 1953]) comparable to the wavelength of the incoming light.

References

David A Atchison and Larry N Thibos. 2016. Optical models of the human eye. *Clinical and Experimental Optometry* 99, 2 (March 2016), 99–106. doi:10.1111/cxo.12352

Francesco Banterle, Alessandro Artusi, Tunç O. Aydin, Piotr Didyk, Elmar Eisemann, Diego Gutierrez, Rafal Mantiuk, and Karol Myszkowski. 2011. Multidimensional image retargeting. In *SIGGRAPH Asia 2011 Courses*. ACM, Hong Kong China, 1–612. doi:10.1145/2077434.2077447

Francesco Banterle, Alessandro Artusi, Kurt Debattista, and Alan Chalmers. 2018. *Advanced High Dynamic Range Imaging* (second ed.). Taylor & Francis, CRC Press, Boca Raton.

L. Bluestein. 1970. A linear filtering approach to the computation of discrete Fourier transform. *IEEE Transactions on Audio and Electroacoustics* 18, 4 (Dec. 1970), 451–455. doi:10.1109/TAU.1970.1162132

Daniel Claus and John Marius Rodenburg. 2015. Pixel size adjustment in coherent diffractive imaging within the Rayleigh–Sommerfeld regime. *Applied Optics* 54, 8 (March 2015), 1936. doi:10.1364/AO.54.001936

Omar Cornut. 2024. Dear ImGui. https://github.com/ocornut/imgui Published: GitHub repository.

James A. Ferwerda, Sumanta N. Pattanaik, Peter Shirley, and Donald P. Greenberg. 1996. A model of visual adaptation for realistic image synthesis. In *Proceedings of the 23rd Annual Conference on Computer Graphics and Interactive Techniques (SIGGRAPH '96)*. Association for Computing Machinery, New York, NY, USA, 249–258. doi:10.1145/237170.237262

Andrew S. Glassner. 2004. *Principles of Digital Image Synthesis* (second ed.). Morgan Kaufmann, San Francisco, Calif.

Joseph W. Goodman. 2017. *Introduction to Fourier Optics* (fourth ed.). W.H. Freeman, Macmillan Learning, New York.

Donald P. Greenberg, Kenneth E. Torrance, Peter Shirley, James Arvo, Eric Lafortune, James A. Ferwerda, Bruce Walter, Ben Trumbore, Sumanta Pattanaik, and Sing-Choong Foo. 1997. A framework for realistic image synthesis. In *Proceedings of the 24th Annual Conference on Computer Graphics and Interactive Techniques (SIGGRAPH '97)*. ACM Press/Addison-Wesley Publishing Co., USA, 477–494. doi:10.1145/258734. 258914

William N. Grimes, Adree Songco-Aguas, and Fred Rieke. 2018. Parallel processing of rod and cone signals: retinal function and human perception. *Annual Review of Vision Science* 4, 1 (Sept. 2018), 123–141. doi:10.1146/annurev-vision-091517-034055

Yanlei Hu, Zhongyu Wang, Xuewen Wang, Shengyun Ji, Chenchu Zhang, Jiawen Li, Wulin Zhu, Dong Wu, and Jiaru Chu. 2020. Efficient full-path optical calculation of scalar and vector diffraction using the Bluestein method. *Light: Science & Applications* 9, 1 (July 2020), 119. doi:10.1038/s41377-020-00362-z

Masanori Kakimoto, Kaoru Matsuoka, Tomoyuki Nishita, Takeshi Naemura, and Hiroshi Harashima. 2004. Glare Generation Based on Wave Optics. In *Proceedings of the*

Fig. 14. Images depicting the incorporation of glare patterns (around the car's specular highlights) into a daytime scene.

Fig. 15. Images depicting the incorporation of glare patterns (around the car headlights) into a nighttime scene.

Computer Graphics and Applications, 12th Pacific Conference (PG '04). IEEE Computer Society, USA, 133–142.

John M. Kessenich, Graham Sellers, and Dave Shreiner. 2017. *OpenGL programming guide: the official guide to learning OpenGL, version 4.5 with SPIR-V* (ninth edition ed.). Addison-Wesley, Boston, MA.

Markus Lendermann, Joel Shi Quan Tan, Jin Ming Koh, and Kang Hao Cheong. 2018. Computational imaging prediction of starburst-effect diffraction spikes. *Scientific Reports* 8, 1 (Nov. 2018), 16919. doi:10.1038/s41598-018-34400-z

Laura R. Luidolt, Michael Wimmer, and Katharina Krosl. 2020. Gaze-dependent simulation of light perception in virtual reality. *IEEE Transactions on Visualization and Computer Graphics* 26, 12 (Dec. 2020), 3557–3567. doi:10.1109/TVCG.2020.3023604

Martin A. Mainster and Patricia L. Turner. 2012. Glare's causes, consequences, and clinical challenges after a century of ophthalmic study. *American Journal of Ophthalmology* 153, 4 (April 2012), 587–593. doi:10.1016/j.ajo.2012.01.008

Eihachiro Nakamae, Kazufumi Kaneda, Takashi Okamoto, and Tomoyuki Nishita. 1990. A lighting model aiming at drive simulators. *ACM SIGGRAPH Computer Graphics* 24, 4 (Sept. 1990), 395–404. doi:10.1145/97880.97922

Merlin Nimier-David, Delio Vicini, Tizian Zeltner, and Wenzel Jakob. 2019. Mitsuba 2: a retargetable forward and inverse renderer. *ACM Trans. Graph.* 38, 6 (Nov. 2019), 1–17. doi:10.1145/3355089.3356498 Place: New York, NY, USA Publisher: Association for Computing Machinery.

Noé Alcalá Ochoa. 2017. Alternative approach to evaluate the Rayleigh-Sommerfeld diffraction integrals using tilted spherical waves. *Optics Express* 25, 10 (May 2017), 12008. doi:10.1364/OE.25.012008

Vitor F. Pamplona, Manuel M. Oliveira, and Gladimir V. G. Baranoski. 2009. Photorealistic models for pupil light reflex and iridal pattern deformation. *ACM Trans. Graph.* 28, 4 (Sept. 2009), 1–12. doi:10.1145/1559755.1559763 Place: New York, NY, USA Publisher: Association for Computing Machinery.

Sumanta N. Pattanaik, James A. Ferwerda, Mark D. Fairchild, and Donald P. Greenberg. 1998. A multiscale model of adaptation and spatial vision for realistic image display. In *Proceedings of the 25th Annual Conference on Computer Graphics and Interactive Techniques (SIGGRAPH '98).* Association for Computing Machinery, New York, NY, USA, 287–298. doi:10.1145/280814.280922

T. Ritschel, M. Ihrke, J. R. Frisvad, J. Coppens, K. Myszkowski, and H.-P. Seidel. 2009. Temporal glare: real-time dynamic simulation of the scattering in the human eye. *Computer Graphics Forum* 28, 2 (April 2009), 183–192. doi:10.1111/j.1467-8659.2009.01357.x

Przemyslaw Rokita. 1993. A model for rendering high intensity lights. *Computers & Graphics* 17, 4 (July 1993), 431–437. doi:10.1016/0097-8493(93)90032-5

Jacob Rubinstein. 2019. On the geometry of visual starbursts. *Journal of the Optical Society of America A* 36, 4 (April 2019), B58. doi:10.1364/JOSAA.36.000B58

Luis Miguel Sanchez-Brea, Angela Soria-Garcia, Joaquin Andres-Porras, Veronica Pastor-Villarrubia, Mahmoud H. Elshorbagy, Jesus Del Hoyo, Francisco Jose Torcal-Milla, and Javier Alda. 2024. Diffractio: an open-source library for diffraction and interference calculations. In *Optics and Photonics for Advanced Dimensional Metrology III*, Peter J. De Groot, Pascal Picart, and Felipe Guzman (Eds.). SPIE, Strasbourg, France, 46. doi:10.1117/12.3021879

Fabin Shen and Anbo Wang. 2006. Fast-Fourier-transform based numerical integration method for the Rayleigh-Sommerfeld diffraction formula. *Applied Optics* 45, 6 (Feb. 2006), 1102. doi:10.1364/AO.45.001102

Mikio Shinya, Takafumi Saito, and Tokiichiro Takahashi. 1989. Rendering techniques for transparent objects. In *Proceedings of the Graphics Interface '89 (GI 1989).* Canadian Information Processing Society, Toronto, Ontario, Canada, 173–182. doi:10.20380/GI1989.24 ISSN: 0713-5424 event-place: London, Ontario, Canada.

G. C. Simpson. 1953. Ocular haloes and coronas. *British Journal of Ophthalmology* 37, 8 (Aug. 1953), 450–486. doi:10.1136/bjo.37.8.450

Greg Spencer, Peter Shirley, Kurt Zimmerman, and Donald P. Greenberg. 1995. Physically-based glare effects for digital images. In *Proceedings of the 22nd Annual Conference on Computer Graphics and Interactive Techniques (SIGGRAPH '95).* Association for Computing Machinery, New York, NY, USA, 325–334. doi:10.1145/218380.218466

Yuxiang Sun and Gladimir Baranoski. 2025. Code for "Glare Pattern Depiction: High-Fidelity Physical Computation and Physiologically-Inspired Visual Response". https://github.com/sunyuxiangyx/glare-sigasia-2025

J. Tumblin and H. Rushmeier. 1993. Tone reproduction for realistic images. *IEEE Computer Graphics and Applications* 13, 6 (Nov. 1993), 42–48. doi:10.1109/38.252554

Thomas J. T. P. van den Berg, Michiel P. J. Hagenouw, and Joris E. Coppens. 2005. The ciliary corona: physical model and simulation of the fine needles radiating from point light sources. *Investigative Opthalmology & Visual Science* 46, 7 (July 2005), 2627. doi:10.1167/iovs.04-0935

Greg Ward. 1994. A contrast-based scalefactor for luminance display. In *Graphics Gems IV.* Academic Press Professional, Inc., USA, 415–421.

Renfeng Xu, Pete Kollbaum, Larry Thibos, Norberto Lopez-Gil, and Arthur Bradley. 2018. Reducing starbursts in highly aberrated eyes with pupil miosis. *Ophthalmic and Physiological Optics* 38, 1 (2018), 26–36. doi:10.1111/opo.12420

Renfeng Xu, Larry N. Thibos, Norberto Lopez-Gil, Pete Kollbaum, and Arthur Bradley. 2019. Psychophysical study of the optical origin of starbursts. *Journal of the Optical Society of America A* 36, 4 (April 2019), B97. doi:10.1364/JOSAA.36.000B97

Yi-rong Yang, Justin Wanek, and Mahnaz Shahidi. 2008. Representing the retinal line spread shape with mathematical functions. *Journal of Zhejiang University SCIENCE B* 9, 12 (Dec. 2008), 996–1002. doi:10.1631/jzus.B0820184